1 # The spectral signature of cloud spatial structure in shortwave

2 # irradiance

3 **Shi Song[1,2], K. Sebastian Schmidt[1,2], Peter Pilewskie[1,2], Michael D. King[2], Andrew K.**

4 **Heidinger[3], Andi Walther[3], Hironobu Iwabuchi[4], Gala Wind[5], Odele M. Coddington[2]**

5 [1] Department of Atmospheric and Oceanic Sciences, University of Colorado, Boulder, CO,

6 USA

7 [2] Laboratory for Atmospheric and Space Physics, University of Colorado, Boulder, CO, USA

8 [3] NOAA Center for Satellite Applications and Research, Madison, WI, USA

9 [4] Center for Atmospheric and Oceanic Studies, Tohoku University, Japan

10 [5] Space Systems and Applications, INC., Greenbelt, MD, USA

13 **Abstract**

14 In this paper, we used cloud imagery from a NASA field experiment in conjunction with three-

15 dimensional radiative transfer calculations to show that cloud spatial structure manifests itself as

16 spectral signature in shortwave irradiance fields – specifically in transmittance and net horizontal

17 photon transport in the visible and near-ultraviolet wavelength range. We found a robust

18 correlation between the magnitude of net horizontal photon transport (H) and its spectral

19 dependence (slope), which is scale-invariant and holds for the entire pixel population of a

20 domain. This was at first surprising given the large degree of spatial inhomogeneity. We prove

21 that the underlying physical mechanism for this phenomenon is molecular scattering in

22 conjunction with cloud spatial structure. On this basis, we developed a simple parameterization

23 through a single parameter ε, which quantifies the characteristic spectral signature of spatial

24 inhomogeneities. In the case we studied, neglecting net horizontal photon transport leads to a

25 local transmittance bias of ±12-19% even at the relatively coarse spatial resolution of 20

26 kilometers. Since three-dimensional effects depend on the spatial context of a given pixel in a

non-trivial way, the spectral dimension of this problem may emerge as the starting point for future bias corrections.

1. Introduction

Determining cloud radiative effects for scenes with a high degree of spatial complexity remains one of the most persistent problems in atmospheric radiation, especially at the surface where satellite observations can only be used indirectly to infer energy budget terms. In the shortwave (solar) spectral range, it is especially challenging to derive consistent albedo, absorption, and transmittance from spaceborne, aircraft, and ground-based observations for inhomogeneous cloud conditions (Kato et al., 2013; Ham et al., 2014). This problem is closely related to the long-debated discrepancy between observed and modeled cloud absorption (Stephens et al., 1990) since energy conservation for a three-dimensional (3D) atmosphere (Marshak and Davis, 2005, Eq. 12.13)

$$R + T = 1 - (A + H) \tag{1}$$

connects reflectance R, transmittance T, and absorptance A of a layer. The term H accounts for lateral net radiative flux from pixel to pixel (which we will call net horizontal photon transport). Out of necessity, most algorithms for deriving R, T, and A from passive imagery inherently presume isolated pixels by relying on one-dimensional (1D) radiative transfer (independent pixel approximation) which does not reproduce H. Net horizontal photon transport has therefore long been a common explanation not only for inconsistencies between measured and calculated broadband cloud absorption (Fritz and MacDonald, 1951; Ackerman and Cox, 1981) but also for remote sensing artifacts (Platnick, 2001).

Observational evidence for this explanation emerged with the availability of spectrally resolved aircraft measurements of shortwave irradiance (Solar Spectral Flux Radiometer, SSFR: Pilewskie et al., 2003). Schmidt et al. (2010) derived *apparent absorption*, the sum of A and H, from irradiance measurements aboard the NASA ER-2 and DC-8 aircraft that flew along a collocated path above and below a heterogeneous anvil cloud during the Tropical Composition,

Cloud and Climate Coupling Experiment (TC^4) (Toon et al., 2010). The results of this study showed that, in absolute terms, H at visible wavelengths (where cloud and gas absorption are negligible) can attain a similar magnitude as the absorbed irradiance A at near-infrared wavelengths. Horizontal photon transport thus has the potential to mimic substantially enhanced absorption. Three-dimensional (3D) calculations confirmed the measurements, and radiative closure was achieved within measurement and model uncertainties without invoking proposed enhanced gas absorption (Arking, 1999) or big cloud droplets (Wiscombe et al., 1984). The results also suggested that the overestimation of absorption would persist even when averaging over long distances as proposed by Titov (1998). This is simply because radiation flight legs are often preferentially targeted at cloudy regions ($\langle H \rangle > 0$) and do not adequately sample clear-sky areas where photons are depleted ($\langle H \rangle < 0$), which is interpreted as *apparent emission* in measurements.

Perhaps the most significant finding by Schmidt et al. (2010) was the distinct spectral shape of H from the near-ultraviolet well into the visible wavelength range, leading to the notion of "colored" net horizontal photon transport (Schmidt et al., 2014). A previous study addressing horizontal photon transport from an energy budget point of view (Kassianov and Kogan, 2002) had focused on the wavelength range of 0.7-2.7 μm, specifically to avoid molecular scattering at shorter wavelengths. Strategies for mitigating the overestimation of cloud absorption (Ackerman and Cox, 1981; Marshak et al., 1999) require that H be more or less constant in the visible wavelength range (Welch et al., 1980), and so the discovery of the spectral dependence of H suggested that they should be applied with caution. For example, Marshak et al. (1999) in their conditional sampling technique required that $H = 0$ for at least two *different* wavelengths. Kindel et al. (2011) applied such a modified scheme for boundary layer clouds.

Further analysis of the relationship between cloud structure and its spectral signature, presented here, revealed a surprisingly robust correlation between the *magnitude* of H and its *spectral slope, dH/dλ*. In the course of this paper, we provide evidence for molecular scattering as the physical mechanism behind this correlation and develop a simple parameterization based on this knowledge. We also examined at which spatial aggregation scale H can be ignored and

1   whether the discovered correlation between H and $dH/d\lambda$ is scale invariant. Finally, we

2   considered the ramifications of our findings on the shortwave surface energy budget.

3   Following this introduction, we provide definitions of relevant terms and explain how H

4   relates to top-of-atmosphere (TOA) and surface cloud radiative effects (CRE). We then discuss

5   the data and model calculations that lay the basis for our study (Sections 3 and 4). In section 5,

6   we discuss the correlations between H and $dH/d\lambda$, followed by the underlying physical

7   mechanism and parameterization presented in Section 6. The discovered relationship is then

8   examined as a function of spatial scale (Section 7) and interpreted in terms of the surface CRE

9   (Section 8). In the conclusions, we discuss the significance of our findings and propose multi-

10 spectral or spectral techniques for deriving first-order correction factors in CRE estimates from

11 space, aircraft, and from the surface that may render 3D calculations unnecessary.

12 **2. Net horizontal photon transport and cloud radiative effect**

13   The instantaneous radiative effect of any atmospheric constituent is the difference of net

14 irradiance (flux density) in its presence (all-sky) and absence (clear-sky). For clouds, we define

15 $$CRE_\lambda = \left[\frac{\left(F_\lambda^\downarrow - F_\lambda^\uparrow\right)_{all-sky}}{F_\lambda^{\downarrow,TOA}} - \frac{\left(F_\lambda^\downarrow - F_\lambda^\uparrow\right)_{clear-sky}}{F_\lambda^{\downarrow,TOA}} \right] \times 100\%, \qquad (2)$$

16 where $F_\lambda^\downarrow$ and $F_\lambda^\uparrow$ are downwelling and upwelling irradiance and their difference is net irradiance.

17 For this paper, we normalize the *absolute* radiative effect by the TOA downwelling irradiance

18 $\left(F_\lambda^{\downarrow,TOA}\right)$ and consider the *relative* radiative effect as percentage of the incident irradiance. Also,

19 we use spectrally resolved rather than broadband quantities, indicated by subscript λ.

20   The TOA shortwave CRE is always negative (*cooling* effect) because the reflected

21 irradiance $F_\lambda^{\uparrow,TOA}$ in presence of clouds is larger than for clear-sky conditions. The surface

22 shortwave CRE is also negative because clouds decrease the transmitted irradiance $F_\lambda^{\downarrow,SUR}$, at

23 least for homogeneous conditions; broken clouds can locally increase surface insolation. In

24 contrast to the shortwave CRE at TOA and at the surface, homogeneous clouds have a *warming*

25 effect on the layer in which they reside. For homogeneous conditions (H=0), this can be

26 quantified in terms of the layer property absorptance

$$A_\lambda = \left[\frac{F_\lambda^{\downarrow,top} - F_\lambda^{\uparrow,top}}{F_\lambda^{\downarrow,top}} - \frac{F_\lambda^{\downarrow,base} - F_\lambda^{\uparrow,base}}{F_\lambda^{\downarrow,top}} \right] \times 100\% \tag{3}$$

2   for a cloud located between h_{top} and h_{base} with the same normalization as used above for the

3   relative CRE. It can be determined from aircraft measurements by collocated legs above and

4   below the cloud (Schmidt et al., 2010). The warming within the layer arises from absorption ($A >$

5   0) primarily in the near-infrared wavelength range (1 μm $< \lambda <$ 4 μm). Similarly, layer

6   transmittance and reflectance are defined as

$$T_\lambda = \left(\frac{F_\lambda^{\downarrow,base}}{F_\lambda^{\downarrow,top}} \right) \times 100\% \tag{4}$$

8   and $R_\lambda = \left(\dfrac{F_\lambda^{\uparrow,top} - F_\lambda^{\uparrow,base}}{F_\lambda^{\downarrow,top}} \right) \times 100\%$. $\tag{5}$

9   Related to layer reflectance is the albedo $\alpha_\lambda = F_\lambda^{\uparrow} / F_\lambda^{\downarrow}$ (identical to R_λ for zero surface albedo).

10   The sum of layer absorptance, transmittance, and reflectance defined in this way is 100% and

11   thus satisfies energy conservation for horizontally homogeneous layers. For individual pixel sub-

12   volumes within an inhomogeneous layer (voxels), A_λ in Eq. (3) can be replaced with $A_\lambda + H_\lambda \equiv$

13   V_λ where V_λ stands for the vertical flux divergence (the net irradiance difference above and below

14   a layer). In this way, energy conservation including horizontal transport [Eq. (1)] is retained.

15   The difference of the CRE at TOA and at the surface from Eq. (2) can be related to Eq. (3)

16   as follows:

$$CRE^{TOA} - CRE^{surface} = \left[\frac{\left(F_\lambda^{net,cloud} - F_\lambda^{net,clear} \right)^{TOA}}{F_\lambda^{\downarrow,TOA}} - \frac{\left(F_\lambda^{net,cloud} - F_\lambda^{net,clear} \right)^{surface}}{F_\lambda^{\downarrow,TOA}} \right] \times 100\% \tag{6a}$$

$$= \left[\frac{\left(F_\lambda^{net,TOA} - F_\lambda^{net,surface} \right)^{cloud}}{F_\lambda^{\downarrow,TOA}} - \frac{\left(F_\lambda^{net,TOA} - F_\lambda^{net,surface} \right)^{clear}}{F_\lambda^{\downarrow,TOA}} \right] \times 100\% \tag{6b}$$

19   The first term inside the brackets of Eq. (6b) is identical to A_λ from Eq. (3) if the boundaries of

20   the layer h_{top} and h_{base} are extended to the TOA and surface, respectively. We denote this by $\hat{A}_\lambda$

and distinguish full-column properties using a caret ($\hat{A}$, $\hat{H}$, $\hat{R}$, $\hat{T}$) from the layer properties that bracket only the cloud itself (*A*, *H*, *R*, *T*). The second term in Eq. (6b) stems from "clear-sky" absorption by atmospheric constituents other than clouds (gases and aerosols). Eq. (6b) can then be re-written as

$$\hat{A}_\lambda = CRE^{TOA} - CRE^{surface} + \left[\frac{\left(F_\lambda^{net,TOA} - F_\lambda^{net,surface} \right)^{clear}}{F_\lambda^{\downarrow,TOA}} \right] \times 100\%$$

(6c)

which simply means that the total atmospheric column absorption comprises contributions from the cloud itself as well as from clear-sky absorption. In presence of horizontal inhomogeneities, the left and right side of Eq. (6c) may be inconsistent unless $\hat{A}_\lambda$ is replaced with $\hat{V}_\lambda = \hat{A}_\lambda + \hat{H}_\lambda$ as above.

Presented in this way, the central role of absorptance and horizontal transport in linking the net irradiances above and below a cloud [Eq. (3)], as well as the TOA and surface CRE [Eq. (6c)], becomes clear. While the global TOA CRE can directly be derived from reflected radiances (Loeb et al., 2005), for example from the Clouds and the Earth's Radiant Energy System (CERES) on the Aqua and Terra satellites (Wielicki et al., 1996), the derivation of the surface CRE also requires the knowledge of atmospheric absorptance or transmittance. In the case of CERES, the required cloud properties are obtained from retrievals of the accompanying imager, the Moderate Resolution Imaging Spectroradiometer (MODIS) (Minnis et al., 2011). As stated in the previous section, this is accomplished through lookup tables which are based on 1D calculations and therefore do not provide *H*.

Recognizing the crucial significance of horizontal photon transport for obtaining an accurate surface CRE, Barker et al. (2012) and Illingworth et al. (2015) described the ambitious goal of using 3D radiative transport operationally in the European radiative budget experiment Earth Clouds, Aerosols and Radiation Explorer (EarthCARE). They tested their algorithm with A-Train data. As a metric for 3D effects, they employed the commonly used difference between 3D and IPA calculations (e.g., Scheirer and Macke, 2003). In a similar manner, Ham et al. (2014) calculated the effect of horizontal photon transport on cloud absorption, transmission, and

1 reflected radiance. They found these three quantities to be correlated when stratifying their results

2 by cloud type after spatial aggregation to at least 5 km.

3 Since the studies cited above pertained to EarthCARE and CERES, they only considered

4 broadband effects. This does not allow distinguishing between A_λ and H_λ by means of their

5 distinct spectral characteristics. Our approach, first presented by Schmidt et al. (2014), bridges

6 this gap. In this paper, we focus exclusively on the near-ultraviolet and visible wavelength range

7 and explore the spectral fingerprint from cloud inhomogeneities in conjunction with molecular

8 scattering in H_λ, which also imprints itself on reflected radiances (Song 2016; Song et al., 2016).

9 We chose not to include aerosols in either study, primarily to isolate the spectral signature of

10 heterogeneous clouds before considering the more general case of clouds and aerosols in

11 combination.

12 **3. Cloud Data**

13 Our study builds upon the results by Schmidt et al. (2010) and therefore uses the same

14 cloud case, a tropical convective core with anvil outflow, observed during the TC[4] experiment on

15 17 July 2007 (from 1519 to 1535 UTC) by the NASA ER-2 aircraft about 300 km south of

16 Panama. Two realizations of the observed cloud field were used as input to 3D radiative transfer

17 calculations, one based on airborne imagery only (as in the earlier study, Section 3.1), and one

18 based on merged airborne and geostationary imagery (Section 3.2) to study large-scale effects.

19 **3.1 Sub-scene from ER-2 passive and active remote sensors**

20 Level-2 cloud retrievals of the Moderate Resolution Imaging Spectrometer (MODIS)

21 Airborne Simulator (MAS: King et al., 1996; King et al., 2010) were combined with reflectivity

22 profiles from the Cloud Radar System (CRS: Li et al., 2004) as described in detail by Schmidt et

23 al. (2010). The primary information originates from MAS optical thickness, thermodynamic

24 phase, effective radius, and cloud top height retrievals for each pixel (x,y) within the imager's

25 swath (roughly 20 km for a cloud top height of 10 km). The imagery-derived information was

26 extended into the vertical dimension z by simple approximations:

27 (1) The effective radius from MAS, $r_e(x,y)$, was used throughout the vertical dimension z

1 although representative only of the topmost layer. Since the study is limited to the near-

2 ultraviolet and visible wavelength range where cloud absorption is negligible, this

3 simplification only affects the scattering phase function. Approximating it with that at

4 cloud top is acceptable because to first approximation, 3D radiative transfer is determined

5 by the distribution of cloud extinction.

6 (2) The MAS-retrieved optical thickness $\tau(x,y)$ for each pixel was vertically distributed by

7 using the water content (WC) profile from CRS: $WC(z) = 0.137 \times Z^{0.64}$ (Liu and

8 Illingworth, 2000) where Z is the radar reflectivity from CRS in dBZ. Since WC(z) is only

9 available along the flight track, nadir-only CRS profiles were also used across the entire

10 MAS swath (shifted vertically by z_0 to match the MAS cloud top height at off-nadir

11 pixels). Cloud extinction β for each voxel (x,y,z) was thus obtained as

12 $$\beta(x,y,z) = \tau_{MAS}(x,y) \times WC(z+z_0) / \sum_z WC(z)_.$$

13 Along the flight track, the mismatch between MAS- and CRS-retrieved cloud top height

14 is $\leqslant$ 0.5 km. The CRS-derived average cloud top height is 10.8 km, and the mean

15 geometrical thickness is 3.3 km.

16 The resulting cloud field was gridded to a resolution of 0.5 km horizontally (similar to the

17 MODIS pixel size of some channels) and 1.0 km vertically (chosen larger than the mismatch

18 between CRS and MAS in cloud top height).

19 Figure 1 shows the cloud optical thickness field from MAS after regridding, with the

20 nadir track highlighted as a dashed line. The length of this scene is 192 km (384 pixels in x), and

21 the width is 17.5 km (35 pixels in y).

22 **3.2 Large-scale field from ER-2 data merged with geostationary imagery**

23 To generalize our findings to larger scales than 17.5 km, we embedded the sub-scene from

24 the ER-2 remote sensors in the context of the large-scale cloud field as retrieved from the

25 Geostationary Operational Environmental Satellite West (GOES-11). The imager onboard

26 GOES-11 has five channels centered at 0.65, 3.9, 6.7, 10.7 and 12.0 μm. In the sampling region,

27 cloud property retrievals were produced at 15:15 and 15:45 UTC (Walther and Heidinger, 2012).

We chose the earlier time because it was more consistent with the MAS retrieval in terms of the optical thickness along the ER-2 track. There are small discrepancies between the GOES and MAS cloud top height retrievals, which are due to a combination of the different spatial resolutions, and channels that are used for the respective retrievals (Walther and Heidinger, 2012; Platnick et al., 2003; King et al., 2010). For the purpose of this study, these differences are not significant.

Figure 2 shows the extended cloud scene (240 km × 240 km). Outside the MAS swath, GOES-11 retrievals were used instead of those from MAS. Similarly, as for the sub-scene cloud, the effective radius retrieval was extended throughout the vertical dimension. The optical thickness was distributed vertically using the CRS profile with the closest match in column-integrated water path (as compared to the retrieved value from GOES) and adjusted in altitude to match the cloud top height retrievals from GOES-11. This approach for distributing profile information from active instrumentation across the swath of a passive imager is more simplistic than that developed by Barker et al. (2011) who used multi-spectral radiances from MODIS. Transferring radar information to off-nadir pixels as far away as 120 km is not necessarily justified due to spatial de-correlation of cloud systems (Miller et al., 2014). However, in the absence of any other information, it was considered the best alternative to estimating the cloud vertical structure without any *a priori* knowledge.

4. Model calculations

The calculations in this study were performed with the 3D Monte Carlo Atmospheric Radiative Transfer Simulator (MCARaTS: Iwabuchi, 2006). MCARaTS is an open-source code written in FORTRAN-90, which can be obtained at sites.google.com/site/mcarats/. It calculates shortwave and longwave spectral or broadband radiances and irradiances based on a forward propagating photon transport algorithm. It is optimized to run efficiently on parallel computers.

In addition to the two 3D cloud fields described in Section 3, the standard tropical summer atmosphere as distributed within the libRadtran radiative transfer package (www.libradtran.org: Mayer and Kylling, 2005) was used to prescribe the vertical profile of temperature, pressure, water vapor, and other atmospheric gases. For gas molecular scattering, we

1 calculated the optical thickness for each layer with the approximation by Bodhaine et al. (1999)

2 and used the built-in Rayleigh scattering phase function from MCARaTS. For gas molecular

3 absorption, we adopted the correlated *k*-distribution method described by Coddington et al.

4 (2008). It was originally based on Mlawer and Clough (1997), modified for the shortwave by

5 Bergstrom et al. (2003), and was specifically developed for the Solar Spectral Flux Radiometer

6 (SSFR: Pilewskie et al., 2003). The SSFR instrument line shape (6-8 nm full-width half-

7 maximum) defines the width of the channels in this study (narrower than MODIS or MAS

8 channels). The spectrum by Kurucz (1992) served as the extraterrestrial solar spectrum.

9 Calculations were performed at eleven wavelengths ranging from the near ultraviolet to

10 the very-near infrared (350, 400, 450, 500, 550, 600, 650, 700, 750, 800, 1000 nm) to capture the

11 spectral dependence of horizontal photon transport over a wide range of molecular scattering. At

12 1000 nm, molecular scattering is negligible and water vapor absorption is small; cloud absorption

13 is negligible for all wavelengths. For pixels dominated by ice clouds, the scattering phase

14 function and single scattering albedo were used from the general habit mixture of the ice cloud

15 bulk models developed by Baum et al. (2011) (parameterized by the effective radius). For liquid

16 water clouds (minority of cloud pixels), single scattering albedo and asymmetry parameter from

17 Mie calculations were used in conjunction with a Henyey-Greenstein phase function (which

18 generally simplifies irradiance calculations). In this study, all calculations were performed for an

19 ocean surface albedo (Coddington et al., 2010) and for a solar zenith angle of 35° for consistency

20 with the earlier publication by Schmidt et al. (2010). The solar azimuth angle was 60° (northeast).

21 The scene parameters (solar geometry, surface albedo, cloud properties) will be generalized in

22 future work (Song, 2016). For each wavelength, 10^{11} (10^{12}) photons were used for the sub-scene

23 (large-scale) cloud field, which corresponds to 7×10^{6} (4×10^{6}) per pixel, respectively. MCARaTS

24 was run in the forward irradiance mode with periodic boundary conditions. For each 3D model

25 run, calculations were also performed using the independent pixel approximation (IPA) where

26 horizontal photon transport is deactivated.

5. Relationship between cloud spatial structure, net horizontal photon transport, and its spectral dependence

This section discusses the relationship between spatial structure and spectrally dependent horizontal photon transport based on the small sub-scene. Since true absorption, A_λ, is negligible, H_λ is equal to V_λ, the vertical flux divergence of an inhomogeneous cloud layer as defined in Section 2, with $h_{top} \approx 13$ km and $h_{base} \approx 8$ km.

Table 1 shows the optical thickness and effective radius for the eight highlighted pixels from Fig. 1 along with H_0, the horizontal photon transport at $\lambda = 500$ nm, expressed in percent of the incident irradiance. Positive values of H_0 are related to net photon loss to other pixels ("radiation donors"), negative values to net photon gain ("radiation recipient" pixels). In the small domain, values as high as 50% and as low as −125% were attained. When H_0 falls below −100%, the radiation received through the sides of a column or voxel exceeds that from the top of the domain. Table 1 is sorted by H_0 rather than by optical thickness. It shows immediately that there is no relationship between the optical thickness (or cloud reflectance) and horizontal photon transport. For example, pixel #6 is a "radiation donor," whereas pixel #4 with roughly the same optical thickness is a recipient. For the extreme case of zero cloud optical thickness, the effect of horizontal photon transport had previously been observed as clear-sky radiance enhancement in the vicinity of clouds (Wen et al., 2007; Kassianov and Ovtchinnikov, 2008; Várnai and Marshak, 2009; Marshak et al., 2014). Statistically, this enhancement is a function of the distance of a pixel to the nearest cloud. However, the horizontal scale of this dependence varies with the spatial context. Consequently, the distance to a certain cloud element cannot generally be used to parameterize 3D cloud effects for individual pixels, whether cloud-free or cloud-covered. This is illustrated when considering pixels #4-#8 in the anvil outflow, which have low optical thickness (around 10) compared to the convective core (optical thickness ≥ 40) overflown from 15.45-15.48 UTC. The small contrasts in optical thickness (reflectance) between the pixels in close proximity tend to drive the sign of H_0 to a greater extent than the exchange of radiation with the (bright) core (for example, #6→#7, #5→#4, #7→#8, but not #5→#6). On the other hand, pixels #2 and #3 have relatively low values of H_0 although they have the largest optical thickness of all eight

1   pixels. While still donors, the magnitude of net horizontal flux to other pixels seems to be

2   diminished by the vicinity to the convective core. Overall, the direction, let alone the magnitude

3   of net horizontal flux, is difficult to predict from the distribution of optical thickness,

4   emphasizing 3D effects as a non-local phenomenon.

5   For the highlighted pixels in Table 1 (#5-#8), Fig. 3a shows the spectral shape of H_λ. The

6   absolute value H_λ increases with wavelength until it reaches an asymptotic value towards near-

7   infrared wavelengths, which we denote H_∞. Donor pixels ($H_\lambda > 0$) are associated with a positive

8   spectral slope, $S_\lambda \equiv dH_\lambda /d\lambda > 0$; recipient pixels have a negative spectral slope. Remote sensing

9   studies (e.g., Marshak et al., 2008; Várnai and Marshak, 2009) had previously established that the

10   above-mentioned *radiance enhancement* for clear-sky pixels near clouds was associated with

11   "apparent bluing," and proposed molecular scattering as the underlying cause for this spectral

12   dependence. To demonstrate that the same effect is at work here, molecular scattering was

13   deactivated in MCARaTS, keeping everything else the same in the calculations. In the resulting

14   spectra (* symbols in Fig. 3a), the wavelength dependence in the near-ultraviolet and visible

15   range disappears almost entirely, suggesting molecular scattering as the primary cause for the

16   spectral shape not only for clear-sky, but also for cloudy pixels. This begs the question (addressed

17   in the next section) of how it is possible to observe such a significant spectral effect for cloudy

18   pixels, given that cloud scattering outweighs molecular scattering by far. After turning molecular

19   scattering off, the remaining variability in H_λ is due to the weak dependence of cloud scattering

20   properties on wavelength and droplet or crystal effective radius, as well as minor gas absorption

21   features. Note that the earlier study by Schmidt et al. (2010) remained inconclusive as to the

22   mechanism of the spectral dependence they observed.

23   To first order, the spectral shape over the range of 350 to 650 nm can be characterized by

24   a single number—the spectral slope at $\lambda = 500$ nm, S_0 (obtained from a linear fit to $H_{\lambda=350-600}$

25   $_{nm}$, included in Fig. 3a). Table 1 lists the value of S_0 for the eight pixels from Fig. 1, whereas Fig.

26   3b depicts the relationship between H_0 and S_0 for *every* pixel. It shows that not only the sign, but

27   also the magnitude of the net horizontal photon transport, is surprisingly well correlated with its

28   slope at 500 nm (in %/100 nm). This suggests that the phenomenon observed by Schmidt et al.

1 (2010) for a few isolated data points is a general occurrence throughout a heterogeneous cloud

2 field. The close relationship between the magnitude and spectral shape of net horizontal photon

3 transport is the basis for the spectral parameterization of H_λ, developed in the next section.

4   In H_0–S_0 space, all IPA calculations (red dots in Fig. 3b) are reduced to the origin because

5 they do not allow horizontal pixel-to-pixel radiation exchange by definition. Owing to periodic

6 boundary conditions, the domain average of H_0 is zero. The calculations without molecular

7 scattering (gray dots) confirm that molecular scattering dominates the spectral shape throughout

8 the domain. The vertical spread of the gray data points is due to the other factors mentioned

9 above (e.g., variability in cloud microphysics). To some extent, it is also apparent in the IPA

10 calculations.

11 **6. Physical mechanism and parameterization**

12   Our interpretation of Fig. 3 is that H_λ can be understood as the combination of two terms:

13 $H_\lambda = H_\infty + \delta(\lambda)$.   (7)

14 1. The constant offset H_∞ is caused by column-to-column radiation exchange between cloud

15   elements. This is illustrated by Fig. 4, which shows the vertical profile of (a) downwelling,

16   (b) net, and (c) upwelling irradiance at 1000 nm wavelength for the cloud field from Fig. 1.

17   A change of net irradiance between altitudes z_0 and z_1 corresponds to net radiation loss or

18   gain within that layer. In this case, the domain-averaged profile of net irradiance (black line

19   in Fig. 4b) decreases slightly near the surface, due to small absorption in the wing of the 936

20   nm water vapor band. When subsampling over columns with a cloud optical thickness $\tau < 1$,

21   or $\tau > 120$, the 3D calculations differ from the IPA calculations because column-to-column

22   radiation transfer is enabled. Above the cloud field, columns with high cloud optical

23   thickness have higher reflectance than the domain average (Fig. 4c) and collectively lose

24   radiation to those with lower optical thickness; the opposite is true below the cloud where

25   columns with high optical thickness have lower transmittance (Fig. 4a). The magnitude of

26   the net horizontal photon transport (the difference of net irradiances at the bottom and top

27   altitude of a layer) increases with the geometrical layer thickness. Fig. 5 conceptually depicts

1   the processes at work. Above clouds, net horizontal photon transport (reflected radiance,

2   projected into a horizontal plane) occurs from the high- to low-reflectance column. Below

3   clouds, the direction is reversed because the transmittance of thin clouds is larger than that of

4   thicker clouds. Note that below $\tau \approx 4$, directly transmitted radiation dominates the

5   downwelling irradiance, and the cloud may not act as a "diffuser" as shown in Fig. 5. The

6   direction of the green arrows is then along the direct beam. This simplified figure should *not*

7   be interpreted to suggest that the net horizontal transport generally occurs along gradients of

8   cloud optical thickness. As stated above, its direction and magnitude depends not only on

9   directly adjacent columns, but also on the large-scale context, which is why a

10 parameterization of 3D cloud effects in clear-sky areas in terms of the distance to the nearest

11 cloud is only possible in a statistical way, but not on an individual pixel basis (Wen et al.,

12 2007). The value of H_∞ can be obtained from H_λ for wavelengths where molecular scattering

13 becomes negligible and where cloud and gas absorption are small compared to H_λ: $A_\lambda \ll H_\lambda$.

14 For the purpose of this study, we chose $\lambda = 1000$ nm: $H_\infty \approx H_{\lambda=1000\text{ nm}}$.

15 2. The spectral perturbation δ_λ, superimposed on H_∞, introduces the wavelength dependence of

16 H_λ. It is perhaps not immediately intuitive why molecular scattering would reduce the

17 magnitude of H_λ as indicated by the symbolic blue arrows in Fig. 5. Molecular scattering

18 essentially reduces the directionality of horizontal photon transport by redistributing

19 radiation, part of which can then be detected as enhanced clear-sky reflectance of clouds

20 (Marshak et al., 2008). A different, secondary process occurs when radiation is scattered out

21 of the direct beam in clear-sky areas into cloud shadows (dashed blue arrow in Fig. 5). It is

22 spectrally dependent as δ_λ but, unlike δ_λ, *independent* of H_∞ and its direction—thus

23 increasing the net radiation under both optically thick and thin clouds. For 550 nm

24 wavelength and shorter (not shown in Figure 4), the net irradiance does indeed increase

25 towards the surface, both for $\tau > 120$ and for $\tau < 1$. This secondary effect is not explicitly

26 captured by the first-order parameterization given below.

27   We express the proportionality of δ_λ to H_∞ as

1     $\delta(\lambda) = -\varepsilon \left(\dfrac{\lambda}{\lambda_0} \right)^{-x} H_\infty \quad (\varepsilon \geq 0, \lambda_0 = 500 \text{ nm}),$ (8)

2   where $(\lambda/\lambda_0)^{-x}$ describes the wavelength dependence, and ε is the constant of proportionality.

3   The layer thickness for which H_λ is derived affects both H_∞ and δ_λ, but only marginally changes

4   the correlation *between* them. Therefore, ε is a general parameter that can be used for relating

5   spatial inhomogeneities and spectral signature of a cloud scene as a whole. It depends on scene

6   parameters such as surface albedo, solar zenith angle, and cloud micro- and macrophysics

7   (including vertical structure). This dependence is explored in a separate publication (Song, 2016).

8   Using Eq. (8), the spectral slope S_0 can be derived as

9     $S_0 = \left. \dfrac{dH_\lambda}{d\lambda} \right|_{\lambda=\lambda_0} = \left. \dfrac{d\delta(\lambda)}{d\lambda} \right|_{\lambda=\lambda_0} = x\varepsilon \dfrac{H_\infty}{\lambda_0},$ (9)

10   By combining Eqs. (7) and (8), one obtains $H_0 = H_{\lambda=500 \text{ nm}} = H_\infty(1 - \varepsilon)$, and Eq. (9) can

11   be rewritten as

12     $S_0 = \dfrac{x\varepsilon}{1-\varepsilon} \dfrac{H_0}{\lambda_0},$ (10)

13   where $x\varepsilon/(1 - \varepsilon)\lambda_0$ is the slope of the linear regression derived using all pixels in the cloud

14   domain (for example, in Fig. 3b). Alternatively, one can derive both ε and x for each individual

15   pixel from the regression of

16     $\log \left(-\dfrac{\delta(\lambda)}{H_\infty} \right) = \log \varepsilon - x \log \dfrac{\lambda}{\lambda_0}$ (11)

17   with $\log \varepsilon$ as intercept and x as slope, as shown in Fig. 6a. In this example, the fit parameter is

18   about 4 as would be expected for molecular scattering as the underlying physical mechanism. The

19   two-dimensional PDF $p(x,\varepsilon)$ for the population of pixels in the domain peaks at $\{x,\varepsilon\} \approx \{3.85,$

20     $0.065\}$ but has a considerable spread in both parameters, which is caused by pixels with

21   negligible horizontal photon transport (and consequently large uncertainties in the fit parameters).

22   The dashed lines in Fig. 3a show the fitted spectra (labeled "theoretical") from this approach. For

23   practical purposes, we fix $x \equiv 4$ for the remainder of this paper. This allows using

1   $$H_\lambda = H_\infty \left(1 - \varepsilon \left(\frac{\lambda}{\lambda_0} \right)^{-4} \right)$$ (12)

2   instead of Eq. (11) and deriving ε and H_∞ for each pixel from a linear regression of H_λ versus

3   $(\lambda/\lambda_0)^{-4}$ (i.e., H_∞ is no longer a required input parameter as for the logarithmic regression). With

4   ε known, S_0 can be calculated from Eq. (9). This is more accurate than the derivation of the slope

5   from a linear fit to the spectrum as used for Fig. 3, which, due to the non-linearity of the spectral

6   dependence, differs from that of the tangent if finite wavelength intervals are used. The domain-

7   wide "effective" ε can then be derived from the slope of the regression line of S_0 versus H_0 for *all*

8   pixels (Eq. (10) with $x = 4$). Fig. 7 shows the distribution of ε as derived from (12) for all those

9   pixels with $\Delta(\varepsilon) < 5\%$. The median of this distribution (0.069) is almost identical to the

10 "effective" value of ε (0.067). The standard deviation of the distribution is about 0.01. This

11 means that the parameterized correlation between net horizontal transport and its spectral

12 dependence can be applied to the domain as a whole as well as for individual pixels; if the

13 spectral shape of H_λ is known, one can infer its magnitude throughout the near-ultraviolet and

14 visible wavelength range. The correlation is robust regardless of the cloud context of a pixel,

15 which is remarkable given the considerable variability in distance-based measures of 3D cloud

16 effects (Várnai and Marshak, 2009).

17   Although our study was instigated by aircraft measurements, its findings are also relevant

18 for satellite-based derivations of cloud radiative effects since the spectral perturbations δ_λ

19 propagate into observed radiances (Song et al., 2016). This may be exploited in future

20 applications for deriving correction terms for 3D radiative effects via their spectral signature.

21   The mean albedo of an inhomogeneous cloud field derived from CERES observations

22 should be fairly insensitive to 3D effects because they are statistically folded into anisotropy

23 models of such scene types (if these empirical models adequately accomplish the radiance-to-

24 irradiance conversion for a range of sun-sensor geometries). By contrast, surface cloud radiative

25 effects are much less constrained by direct CERES observations because cloud transmittance has

26 to be derived from concomitant imagery. This is where biases introduced by H_λ are most

27 significant. For the remainder of this paper, we therefore analyze the significance of H for

1   varying degrees of spatial aggregation (Section 7) and make the connection to cloud

2   transmittance (Section 8).

3   **7. Scale dependence and spatial aggregation**

4   The results presented so far (e.g., in Fig. 3b) are based on calculations at a resolution of

5   0.5 km. The question is whether the correlation between the magnitude and spectral shape of H is

6   scale invariant, and to what extent the effect of horizontal photon transport can be mitigated by

7   spatial aggregation. To answer this question, we successively coarsened the pixel resolution to 15

8   km, the largest super-pixel contained within the MAS swath (Fig. 1). Figure 8a shows that the

9   correlation is indeed independent of the spatial aggregation scale and thus pixel size. The

10   magnitude of H_0 decreases with pixel size: it ranges from +6% to –5% at 15 km resolution (close

11   to CERES for nadir viewing), compared to about ±50% at 1-5 km (resolution of various MODIS

12   level-2 products). Here, we use the large cloud scene (Fig. 2) to estimate for which aggregation

13   scale beyond 15 km the magnitude of H_0 drops below the radiometric uncertainty of typical

14   space- or ground-based radiometers (3-5%), at which point 3D cloud effects become insignificant

15   from a practical point-of-view.

16   The results for the large scene, shown in Fig. 8b, confirm that the correlation is preserved

17   for scales up to 70 km. However, H_0 at 15 km resolution varies from +17% to –13% throughout

18   the large-scene domain, much more than in the MAS-only domain (+6% to –5%). One

19   explanation for this larger range is the greater complexity of the large domain, providing a more

20   extensive sample of cloud variability than the smaller sub-scene. This becomes quite clear when

21   looking at the spatial distribution of horizontal photon transport: In Fig. 8c, we chose to plot S_0

22   (y-axis in Fig. 8b) rather than H_0. They are practically interchangeable thanks to the correlation

23   between the two. The distribution of effective donor, recipient, and neutral regions (red, blue,

24   green, respectively) bears almost no resemblance to the optical thickness field from Fig. 2. This

25   demonstrates once again that horizontal photon transport cannot be derived from the spatial

26   distribution of clouds in any simple way; strong contrasts between negative and positive H_0 (or

27   S_0) can arise in optically thin boundary layer clouds (southwest corner of Fig. 2 and 8c) as well as

28   in optically thick areas (deep convection, northeast corner of cloud scene). Considering the

1 GOES-MAS large-scene results within the boundaries of the MAS swath only (marked by the

2 green rectangle in Fig. 8c) allows estimating the net exchange of radiation between the MAS

3 domain and its large-scene context. The average value of H_0 within the small-scene subset is

4 +7.9%, which means that the small scene effectively loses photons to its surroundings. This

5 would not be detectable for such a large aggregation scale (where the entire MAS domain

6 represents a single "super-pixel"). This net energy export is not reproduced by the calculations

7 based on the MAS-only domain where the mean value of H_0 is zero, in keeping with energy

8 conservation that is satisfied by periodic boundary conditions in the radiative transfer model. The

9 range of H_0 in the MAS-only sub-scene of the GOES-MAS scene is +17% to –6% at 15 km

10 aggregation scale. This is still a larger range than obtained from the MAS-only calculations (+6%

11 to –5%), even after sub-setting the results from the large scene to the boundaries of the small

12 ones. The reason is simply that the 15 km super-pixel size is already half the width of the MAS-

13 only domain. Boundary conditions enforce the convergence of H_0 to zero as the area ratio of pixel

14 to domain size approaches 1, which causes an underestimation of the variability of H_0 for large

15 aggregation scales. By contrast, photons can also travel outside the confines of the domain in the

16 real world as represented by the larger GOES-MAS cloud scene in our study.

17 This is illustrated in Figure 8d, which shows the range of H_0 for both the large and the

18 small cloud scene as a function of aggregation scale. At small scales, the range is comparable for

19 the small and large scene. At 15 km aggregation scale, the range obtained from the small scene

20 has decreased to about half that of the large one. At 50 km pixel resolution, H_0 ranges from +7%

21 to –3% (+5% to –1% at 70 km). It is likely that the boundary conditions imposed on the large

22 domain also cause an underestimation of the H_0 variability at these large scales. Nevertheless,

23 these results suggest that above 60 km super-pixel size (about 3 × 3 CERES nadir footprints),

24 horizontal photon transport can be neglected for this cloud scene, based on a 3% uncertainty

25 threshold. This is only true when aggregating all native-resolution pixels, regardless of whether

26 they are flagged as clear sky or as cloud-covered. However, sampling cloudy and clear pixels

27 *separately* would result in much larger biases than 3% because high optical thickness pixels are

28 more likely to be effective photon donors than low-optical thickness or clear pixels, causing an

1   asymmetry in the distribution of H_0 (Song et al., 2016).

8. Significance for Cloud Radiative Effect

3   In this section, we evaluate the ramifications of net horizontal photon transport on

4   estimates of cloud radiative effects. For any atmospheric column, H is connected to R and T

5   through Eq. (1) and manifests itself in a transmittance and reflectance bias (λ index omitted):

6    $$\Delta T = T^{IPA} - T^{3D} \tag{13a}$$

7    $$\Delta R = R^{IPA} - R^{3D}. \tag{13a}$$

8   Juxtaposing energy conservation for a horizontally homogeneous atmosphere ($T^{IPA} + R^{IPA} = 1$)

9   with Eq. (1) for conservative scattering ($A=0$, therefore $T^{3D} + R^{3D} = 1 - H$) yields the plausible

10   relationship

11   $$H = \Delta T + \Delta R, \tag{14}$$

12   which means that the error introduced by horizontal photon transport is partitioned into

13   transmittance and reflectance bias. Since the bias ΔR is folded into the empirical radiance-to-

14   irradiance conversion employed by CERES, we focus on ΔT in this study.

15   For the eight super-pixels #11–#18 from Fig. 2, Fig. 9a shows the IPA bias ΔT, ranging

16   from +2% to +14% in the mid-visible. Its spectral dependence is more complicated than the one

17   shown for H in Fig. 3a, with a less obvious correlation between magnitude and spectral shape.

18   Nevertheless, Fig. 9b shows a remarkable correlation between H_0 and ΔT_0 ($T^{IPA} - T^{3D}$ at 500

19   nm) for the same aggregation scales as in Fig. 8b. For example, the H_0 range of +15% to −10%

20   translates into +19% to −12% in ΔT_0 for a horizontal resolution of 20 km. Linear regression

21   between H_0 and ΔT_0 suggests that in this case, H_0 propagates mainly into ΔT_0, whereas it is

22   uncorrelated with ΔR_0 for scales below 20 km (Fig. 10).

23   For simplicity, the spectral dependence of ΔT as shown in Fig. 9a is approximated by

24   $$\Delta T_\lambda = T_\lambda^{IPA} - T_\lambda^{3D} = \xi_0\big|_{350-600nm} \times (\lambda - \lambda_0) + (T_0^{IPA} - T_0^{3D}) \; ; \lambda_0 = 500 \text{ nm} \tag{15}$$

25   where ξ_0 is the spectral slope of $T_\lambda^{IPA} - T_\lambda^{3D}$ calculated from the spectrum between 350 and 600

26   nm. Fig. 9c shows that the spectral slopes of H and ΔT, S_0 and ξ_0, are correlated despite the more

1   complicated spectral dependence of T compared to that of H (Fig. 9a). However, there is clearly

2   no 1:1 relationship as found between H_0 and ΔT_0 above. For example, $S_0 = -10\%/100$ nm

3   corresponds to only $\xi_0 = -6\%/100$ nm. This changes when extending the vertical layer boundaries

4   (8-13 km so far, bracketing only the cloud layer itself) to the atmosphere reaching from the

5   ground to cloud top. This distinction is indicated by carets above all quantities. This is slightly

6   different from the definition of $\hat{T}$ in Section 2 where the upper boundary is the top of

7   atmosphere, not the top of the cloud. Fig. 9d not only shows a much stronger spectral dependence

8   of $\Delta\hat{T}$ (surpassing that of $\hat{H}$) compared to that of ΔT and H in Fig. 9c, but also that the

9   correlation is no longer scale invariant. This means that the vertical bracket for deriving T, R, and

10   H has to be chosen with consideration of the vertical location of the cloud layer. By contrast, the

11   correlation between H and S as discussed in Section 6 is fairly independent of the layer

12   boundaries.

13   For future studies of IPA-3D biases in satellite-derived estimates of surface cloud

14   radiative effects, Fig. 4b suggests the center of a cloud as upper boundary of the bracket where

15   $\left| dF_{net} / dz \right|$ reaches a domain-wide minimum because 3D effects can be vertically separated into a

16   transmittance and reflectance part below and above this level, respectively. Moreover, the

17   correlation between ΔT and its spectral dependence ξ_0 (not shown) can be exploited to detect

18   IPA-3D biases in ground-based irradiance measurements below cloud fields (Song, 2016). While

19   our study suggests that horizontal photon transport mainly propagates into transmittance biases,

20   there is some indication (Fig. 10) that at scales above 20 km, non-zero values of H_0 translate into

21   albedo (reflected irradiance) biases as well. This increasing correlation with scale is probably

22   associated with the gradual de-correlation between $\hat{S}_0$ and $\hat{\xi}_0$ observed in Fig. 9b. In order to

23   improve satellite-based estimates of cloud radiative effects, it is important to understand how H_0

24   is partitioned into ΔT and ΔR [Eq. (14)] at different aggregation scales. A detailed study would

25   need to be conducted for different cloud morphologies, sun angles, and surface albedos and is left

26   for the future.

27   **9. Summary and conclusions**

28   Deriving the radiative effects of inhomogeneous cloud scenes from observations by

1   satellite, aircraft, or at the surface is often portrayed as an intractable problem because it cannot

2   be accomplished by isolating a pixel from its spatial context. At the core of the issue is pixel-to-

3   pixel exchange of radiation, or net horizontal photon transport, which occurs over a range of

4   scales. The original motivation for this study was to gain a physical understanding of this

5   phenomenon's spectral dependence in the near-ultraviolet and visible wavelength range, which

6   had been found in aircraft irradiance observations (Schmidt et al., 2010). We were able to identify

7   molecular scattering as the underlying mechanism for the spectral dependence using three-

8   dimensional radiative transfer calculations with cloud imagery and radar observations as input.

9   When de-activating molecular scattering in the radiative transfer model, the wavelength

10   dependence disappeared almost entirely in the vertical flux divergence V, which comprises net

11   horizontal flux density H as well as true layer absorption A. To simplify the analysis, we limited

12   our study to conservative scattering by choosing wavelengths with negligible gas or cloud

13   absorption ($A \approx 0$), and by excluding aerosols. When activated in the model, molecular scattering

14   manifested itself as a spectral perturbation (more accurately: modulation) δ_λ to an otherwise

15   *spectrally neutral* horizontal flux density H_∞, which in turn could be traced back to horizontal

16   exchange of radiation due to spatial inhomogeneity of cloud elements within the domain. Beyond

17   the original scope of this study, we made a few surprising discoveries:

18   1.   The spectral perturbation δ_λ is not independent of the spectrally neutral part H_∞ caused by

19   the clouds themselves. Instead, the mid-visible spectral slope of H_λ is correlated with H itself

20   (i.e., with the magnitude of the spectrally neutral part H_∞), which led to the simple

21   parameterization

$$\delta_\lambda = -\varepsilon \left(\frac{\lambda}{\lambda_0} \right)^{-x} H_\infty \, .$$

23   2.   We were able to show that the exponent x is close to 4, which further confirmed molecular

24   scattering as the dominating physical mechanism behind the spectral perturbation. The

25   constant of proportionality, ε, can be regarded as universally valid for all pixels within the

26   cloud domain, independently of the vertical or horizontal spatial distribution of clouds. This

27   means that the spectrally dependent horizontal photon transport can be represented as

$$1 \qquad H_\lambda = H_\infty + \delta_\lambda = H_\infty \left(1 - \varepsilon \left(\frac{\lambda}{\lambda_0} \right)^{-4} \right)$$

2   for *each pixel* within the domain with $\varepsilon = 0.7 \pm 0.1$ for the scene we studied. It seems

3   remarkable that one single value of ε should suffice to describe the relationship between the

4   magnitude of H (caused by clouds) and its spectral dependence (imprinted on H by a

5   completely different physical process, molecular scattering) – especially considering the

6   range of different clouds within the domain. The correlation holds for each pixel, no matter

7   what its spatial context may be. Once ε is established for a given cloud scene, the spectral

8   perturbations associated with horizontal photon transport can be derived for each pixel if the

9   value of H_0 is known. Conversely, if the spectral shape of H_λ is known at one wavelength, its

10 magnitude can easily be inferred for the whole spectrum. This may be especially significant

11 considering that H cannot be directly observed from space. It is likely that the spectral

12 perturbations will propagate into the observed radiances. Indeed, Song et al. (2016) found

13 evidence of this connection in aircraft data, which had previously been reported by Várnai

14 and Marshak (2009) in clear-sky satellite observations near clouds. The close correlation that

15 we found in our study may be a future pathway to inferring the magnitude of H from its

16 spectral manifestation in the observed radiances.

17 3. The correlation and parameterization hold for a range of spatial aggregation scales, and are

18   fairly independent of the location of the bracketing altitudes that define the layer. This scale

19   invariance only breaks down when extending a layer very close to the surface where a

20   secondary spectral effect has to be factored in (see Section 6 and dashed arrow in Figure 5).

21 4. The observed correlation between H and its spectral shape can also be found between

22   transmitted irradiance T and its spectral shape, although it is not scale invariant beyond

23   20 km.

24 5. H is correlated with ΔT, the IPA transmittance bias for each pixel, but not with ΔR (at least at

25   small scales). This means that 3D cloud effects in the form of horizontal photon transport

26   translate almost exclusively into a transmittance bias. At scales above 20 km, a correlation

27   between H and ΔR does emerge, which requires further study. The correlation between H

and ΔT can potentially be exploited for ground-based spectral irradiance observations (Song, 2016).

Few of these findings could be expected at the outset of our research, and they evoke a number of new questions:

1. How does the discovered correlation and the constant of proportionality in its parameterization, ε, depend on scene parameters such as solar zenith and azimuth angle, surface albedo (magnitude and spectral dependence), and cloud morphology and microphysics? What "drives" the parameter ε?

2. Can the spectral perturbations associated with H indeed be detected in reflected radiances, and can they be used to infer the magnitude of H indirectly?

3. Can the findings for the near-ultraviolet and visible wavelength range be generalized to the near-infrared wavelength range where clouds and atmospheric gases do absorb?

4. What are the implications of our findings for estimating aerosol radiative effects (such as heating rates) in presence of inhomogeneous cloud fields?

5. Can the method by Ackerman and Cox (1981) to correct for horizontal photon transport in aircraft measurements of atmospheric absorption by using a visible channel as basis for the correction of near-infrared absorption be upheld for future measurements, even in the modified form proposed by Kassianov and Kogan (2002)?

6. Can H and ΔT be derived from spectral perturbations in transmitted irradiance observations by ground-based spectrometers?

Question 2 will be partially addressed by Song et al. (2016); questions 1, 3, 5, and 6 are discussed by Song (2016) and will be further investigated in future publications. Furthermore, questions 3 and 4 are the subjects of active research in the framework of an ongoing or planned field missions (NASA ORACLES and CAMP2Ex). This publication constitutes a further contribution to the emerging field of cloud-aerosol spectroscopy (Schmidt and Pilewskie, 2012), which is expected to improve the estimation of cloud-aerosol parameters and their radiative effects through spectrally resolved observations from the ground, aircraft, and, ultimately, space.

1   **Acknowledgements**

2   The research presented in this paper was supported by grants NNX14AP72G (Shi Song and

3   Sebastian Schmidt) and NNX12AC41G (Michael King) within the NASA radiation sciences

4   program. The calculations were performed on the supercomputer "Janus", which is supported by

5   the US National Science Foundation (award number CNS-0821794) and the University of

6   Colorado Boulder. It is a joint effort of the University of Colorado Boulder, the University of

7   Colorado Denver, and the National Center for Atmospheric Research. Janus is operated by the

8   University of Colorado Boulder. We appreciate the effort of Thomas Arnold (NASA Goddard

9   Space Flight Center) in supporting the MAS calibrations and retrievals.

References

Ackerman, S. A., and Cox, S. K.: Aircraft observations of shortwave fractional absorptance of non-homogeneous clouds, J. Appl. Meteorol., 20, 1510-1515, 1981.

Arking, A.: The influence of clouds and water vapor on atmospheric absorption, Geophys. Res. Lett., 26, 2729-2732, 1981.

Barker, H. W., Jerg, M. P., Wehr, T., Kato, S.: Donovan D. P., and Hogan R. J.: A 3D cloud-construction algorithm for the EarthCARE satellite mission. Q. J. Roy. Meteorol. Soc., 137, 1042-1058, 2011.

Barker, H. W., Kato, S., and Wehr, T.: Computation of solar radiative fluxes by 1D and 3D methods using cloudy atmospheres inferred from A-train satellite data, Surv. Geophys., 33, 657–676, 2012.

Baum, B. A., Yang, P., Heymsfield, A. J., Schmitt, C., Xie, Y., Bansemer, A., Hu, Y. X., and Zhang, Z.: Improvements to shortwave bulk scattering and absorption models for the remote sensing of ice clouds. J. Appl. Meteor. Climatol., 50, 1037-1056, 2011.

Bergstrom, R. W., Pilewskie, P., Schmid, B., and Russell, P. B.: Estimates of the spectral aerosol single scattering albedo and aerosol radiative effects during SAFARI 2000, J. Geophys. Res., 108, 8474, doi:10.1029/2002JD002435, 2003.

Bodhaine, B. A., Wood, N. B., Dutton, E. G., and Slusser, J. R.: On Rayleigh optical depth calculations, J. Atmos. and Ocean. Tech., 16, 1854-1861, 1999.

Coddington, O., Schmidt, K. S., Pilewskie, P., Gore, W. J., Bergstrom, R. W., Roman, M., Redemann, J., Russell, P. B., Liu, J., and Schaaf, C. C.: Aircraft measurements of spectral surface albedo and its consistency with ground-based and space-borne observations, J. Geophys. Res., 113, D17209, doi:10.1029/2008JD010089, 2008.

Coddington, O. M., Pilewskie, P., Redemann, J., Platnick, S., Russell, P. B., Schmidt, K. S., Gore, W. J., Livingston, J., Wind, G., and Vukicevic, T.: Examining the impact of overlying aerosols on the retrieval of cloud optical properties from passive remote sensing, J. Geophys. Res., 115, D10211, doi:10.1029/2009JD012829, 2010.

Fritz, S., and MacDonald, T. H.: Measurements of absorption of solar radiation by clouds, Bull.

Am. Meteorol. Soc., 32, 205-209, 1951.

Ham, S.-H., Kato, S., Barker, H. W., Rose, F. G., and Sun-Mack, S.: Effects of 3-D clouds on atmospheric transmission of solar radiation: Cloud type dependencies inferred from A-train satellite data, J. Geophys. Res., 119, 943-963, 2014.

Illingworth, A. J., Barker, H. W., Beljaars, A., Ceccaldi, M., Chepfer, H., Clerbaux, N., Cole, J., Delanoë, J., Domenech, C., Donovan, D. P., Fukuda, S., Hirakata, M., Hogan, R. J., Huenerbein, A., Kollias, P., Kubota, T., Nakajima, T., Nakajima, T. Y., Nishizawa, T., Ohno, Y., Okamoto, H., Oki, R., Sato, K., Satoh, M., Shephard, M. W., Velázquez-Blázquez, A., Wandinger, U., Wehr, T., and van Zadelhoff, G.-J.: The EarthCARE Satellite: The Next Step Forward in Global Measurements of Clouds, Aerosols, Precipitation, and Radiation. Bull. Amer. Meteor. Soc., 96, 1311–1332, doi: http://dx.doi.org/10.1175/BAMS-D-12-00227.1, 2015.

Iwabuchi, H.: Efficient Monte Carlo methods for radiative transfer modeling. J Atmos. Sci., 63, 2324-2339, 2006.

Kassianov, E. I., and Kogan, Y. L.: Spectral dependence of radiative horizontal transport in stratocumulus clouds and its effect on near-IR absorption, J. Geophys. Res., 107(D23), 4712, doi:10.1029/2002JD002103, 2002.

Kassianov E. I., and Ovtchinnikov, M.: On reflectance ratios and aerosol optical depth retrieval in the presence of cumulus clouds. Geophys. Res. Lett., 35:L06807. http://dx.doi.org/10.1029/2008GL033231, 2008.

Kato, S., Loeb, N. G., Rose, F. G., Doelling, D. R., Rutan, D. A., Caldwell, T. E., Yu, L., and Weller, R. A.: Surface irradiances consistent with CERES-derived top-of-atmosphere shortwave and longwave irradiances, J. Clim., 26, 2719-2740, 2013.

Kindel, B. C., Schmidt, K. S., Pilewskie, P., Baum, B. A., Yang, P., and Platnick, S.: Observations and modeling of ice cloud shortwave spectral albedo during the Tropical Composition, Cloud and Climate Coupling Experiment (TC[4]), J. Geophys. Res., 115, D00J18, doi:10.1029/2009JD013127, 2010.

Kindel, B. C., Pilewskie, P., Schmidt, K. S., Coddington, O. M., and King, M. D.: Solar spectral

absorption by marine stratus clouds: Measurements and modeling, J. Geophys. Res., 116, D10203, doi:10.1029/2010JD015071, 2011.

King, M. D., Menzel, W. P., Grant, P. S., Myers, J. S., Arnold, G. T., Platnick, S. E., Gumley, L. E., Tsay, S. C., Moeller, C. C., Fitzgerald, M., Brown, K. S., and Osterwisch, F. G.: Airborne scanning spectrometer for remote sensing of cloud, aerosol, water vapor and surface properties, J. Atmos. Ocean. Tech., 13, 777-794, 1996.

King, M. D., Platnick, S., Wind, G., Arnold, G. T., and Dominguez, R. T.: Remote sensing of radiative and microphysical properties of clouds during TC[4]: Results from MAS, MASTER, MODIS, and MISR, J. Geophys. Res, 115, D00J07, doi:10.1029/2009JD013277, 2010.

Kurucz, R. L.: Synthetic infrared spectra, in Infrared Solar Physics: Proceedings of the 154th Symposium of the International Astronomical Union, edited by D. M. Rabin, J. T. Jefferies, and C. Lindsey, pp. 523-531, Kluwer Acad., Dordrecht, Netherlands, 1992.

Li, L., Heymsfield, G. M., Racette, P. E., Tian, L., and Zenker, E.: A 94 GHz cloud radar system on a NASA high-altitude ER-2 aircraft, J. Atmos. Oceanic Technol., 21, 1378-1388, 2004.

Liu, C., and Illingworth, A.: Toward more accurate retrievals of ice water content from radar measurements of clouds, J. Appl. Meteorol., 39, 1130-1146, 2000.

Loeb N. G., Kato, S., Loukachine, K., and Smith, N. M.: Angular distribution models for top-of-atmosphere radiative flux estimation from the clouds and the earth's radiant energy system instrument on the Terra satellite. Part I: Methodology, J Atmos. Oceanic Technol. 22, 338-351, 2005.

Marshak, A., and Davis, A.: 3-D Radiative Transfer in Cloudy Atmospheres, Springer, ISBN-13 978-3-540-23958-1, 2005.

Marshak, A., Platnick, S., Várnai, T., Wen, G., and Cahalan, R. F.: Impact of three-dimensional radiative effects on satellite retrievals of cloud droplet sizes, J. Geophys. Res., 111, D09207, doi:10.1029/ 996 2005JD006686, 2006.

Marshak, A., Wen, G., Coakley, J. A., Jr., Remer, L. A., Loeb, N. G., and Cahalan, R. F.: A simple model for the cloud adjacency effect and the apparent bluing of aerosols near clouds, J. Geophys. Res., 113, D14S17, doi:10.1029/2007JD009196, 2008.

1 Marshak, A., Wiscombe, W., Davis, A., Oreopoulos, L., and Cahalan, R.: On the removal of the
2   effect of horizontal fluxes in two-aircraft measurements of cloud absorption, Quart. J. Roy.
3   Meteorol. Soc., 125, 2153–2170, 1999.

4 Marshak, A., Evans, F. E., Várnai, T., Wen, G.: Extending 3D near-cloud corrections from
5   shorter to longer wavelengths, J. Quant. Spectroscopy 147, 79-85, 2014.

6 Mayer, B., and Kylling, A.: Technical note: The libRadtran software package for radiative
7   transfer calculations—Description and examples of use, Atmos. Chem. Phys., 5, 1855-1877,
8   2005.

9 Miller, S. D., Forsythe, J. M., Partain, P. T., Haynes, J. M., Bankert, R. L., Sengupta, M.,
10   Mitrescu, C., Hawkins, J. D., and Vonder Haar, T. H.: Estimating three-dimensional cloud
11   structure via statistically blended satellite observations. J. Appl. Meteor. Climatol., 53, 437-
12   455, 2014.

13 Minnis, P., Sun-Mack, S., Young, D. F., Heck, P. W., Garber, D. P., Chen, Y., Spangenberg, D.
14   A., Arduini, R. F., Trepte, Q. Z., Smith, W. L. Jr., Ayers, J. K., Gibson, S. C., Miller, W. F.,
15   Hong, G., Chakrapani, V., Takano, Y., Liou, K. N., Xie, Y., and Yang, P.: CERES edition-2
16   cloud property retrievals using TRMM VIRS and Terra and Aqua MODIS data—Part I:
17   Algorithms, IEEE Trans. Geosci. Remote Sens., 49(11), 4374–4400, 2011.

18 Mlawer, E., and Clough, S. A.: On the extension of rapid radiative transfer model to the
19   shortwave region, in Proc. Sixth ARM Science Team Meeting, pp. 223–226, Atmospheric
20   Radiation Measurement (ARM) Program, San Antonio, TX, conf–9603149, 1997.

21 Pilewskie, P., Pommier, J., Bergstrom, R., Gore, W., Rabbette, M., Howard, S., Schmid, B., and
22   Hobbs, P. V.: Solar spectral radiative forcing during the South African Regional Science
23   Initiative, J. Geophys. Res., 108, 8486, doi:10.1029/2002JD002411, 2003.

24 Platnick, S.: Approximations for horizontal photon transport in cloud remote sensing problems, J.
25   Quant. Spectrosc. Radiat. Transfer, 68(1), 75-99, 2001.

26 Platnick, S., M. D. King, S. A. Ackerman, W. P. Menzel, B. A. Baum, J. C. Riedi, and R. A.
27   Frey, 2003: The MODIS cloud products: Algorithms and examples from Terra. IEEE Trans.
28   Geosci. Remote Sens., 41, 459–473.

1   Scheirer, R., and Macke, A.: Cloud inhomogeneity and broadband solar fluxes, J. Geophys. Res.,

2   108, 4599, doi:10.1029/2002JD003321, D19, 2003.

3   Schmidt, K. S., Venema, V., Di Giuseppe, F., Scheirer, R., Wendisch, M., and Pilewskie, P.:

4   Reproducing cloud microphysical and irradiance measurements using three 3D cloud

5   generators, Quart. J. Roy. Meteorol. Soc., 133, 765-780, 2007a.

6   Schmidt, K. S., Pilewskie, P., Platnick, S., Wind, G., Yang, P., and Wendisch, M.: Comparing

7   irradiance fields derived from Moderate Resolution Imaging Spectroradiometer airborne

8   simulator cirrus cloud retrievals with solar spectral flux radiometer measurements, J.

9   Geophys. Res., 112, D24206, doi:10.1029/2007JD008711, 2007b.

10 Schmidt, K. S., Pilewskie, P., Mayer, B., Wendisch, M., Kindel, B., Platnick, S., King, M. D.,

11   Wind, G., Arnold, G. T., Tian, L., Heymsfield, G., and Kalesse, H.: Apparent absorption of

12   solar spectral irradiance in heterogeneous ice clouds, J. Geophys. Res., 115, D00J22,

13   doi:10.1029/2009JD013124, 2010.

14 Schmidt, K. S., and Pilewskie, P.: Airborne Measurements of Spectral Shortwave Radiation in

15   Cloud and Aerosol Remote Sensing and Energy Budget Studies, in Light Scattering

16   Reviews, 6, A. Kokhanovsky (ed.), Springer, 2012.

17 Schmidt, K. S., Song, S., Feingold, G., Pilewskie, P., Coddington, O., 2014: Relating shortwave

18   passive remote sensing and radiative effects if aerosol-immersed broken cloud fields, *AMS*

19   *conference, Boston, July 2014*.

20   https://ams.confex.com/ams/14CLOUD14ATRAD/webprogram/Paper250570.html

21 Stephens, G. L., Tsay, S.-C., Stackhouse Jr., P. W., and Flatau, P. J.: The relevance of the

22   microphysical and radiative properties of cirrus clouds to climate and climatic feedback, J.

23   Atmos. Sci., 47, 1742-1753, 1990.

24 Song, S., Schmidt, K. S., Pilewskie, P., King, M. D., and Platnick, S.: Quantifying the spectral

25   signature of heterogeneous clouds in shortwave radiation measurements during the Studies

26   of Emissions and Atmospheric Composition, Clouds and Climate Coupling by Regional

27   Surveys (SEAC^{4}RS), to be submitted to J. Geophys. Res., 2016.

28 Song, S.: The spectral signature of cloud spatial structure in shortwave radiation. *Ph.D. thesis*,

Department of Atmospheric and Oceanic Sciences, University of Colorado Boulder, USA, 138 pp., 2016.

Titov, G. A.: Radiative horizontal transport and absorption in stratocumulus clouds, J. Atmos. Res., 55, 2549-2560. 1998.

Toon O. B., Starr, D. O., Jensen, E. J., Newman, P. A., Platnick, S., Schoeberl, M. R., Wennberg, P. O., Wofsy, S. C., Kurylo, M. J., Maring, H., Jucks, K. W., Craig, M. S., Vasques, M. F., Pfister, L., Rosenlof, K. H., Selkirk, H. B., Colarco, P. R., Kawa, S. R., Mace, G. G., Minnis, P., and Pickering, K. E.: Planning, implementation, and first results of the Tropical Composition, Cloud and Climate Coupling Experiment (TC[4]), J. Geophys. Res., 115, D00J04, doi:10.1029/2009JD013073, 2010.

Várnai, T., and Marshak, A.: MODIS observations of enhanced clear sky reflectance near clouds, Geophys. Res. Lett., 36, L06807, doi:10.1029/2008GL037089, 2009.

Walther, A., and Heidinger, A.: Implementation of the Daytime Cloud Optical and Microphysical Properties Algorithm (DCOMP) in PATMOS-x. J. Appl. Meteor. Climatol., 51, 1371-1390, 2012.

Welch, R. M., Cox, S. K. and Davis, J. M.: Solar Radiation and Clouds. Meteor. Monogr., No. 39, Amer. Meteor. Soc., 93 pp., 1980.

Wen, G., Marshak, A., Cahalan, R. F., Remer, L. A., and Kleidman, R. G.: 3-D aerosol-cloud radiative interaction observed in collocated MODIS and ASTER images of cumulus cloud fields, J. Geophys. Res.,112, D13204, doi:10.1029/2006JD008267, 2007.

Wielicki, B. A., Barkstrom, B. R., Harrison, E. F., Lee, R. B., Smith, G. L., and Cooper, J. E.: Clouds and the Earth's Radiant Energy System (CERES): An Earth Observing System Experiment, Bull. Amer. Meteor. Soc., 77, 853-868, 1996.

Wiscombe, W. J., Welch, R. M., and Hall, W. D.: The effects of very large drops on cloud absorption, part I: Parcel models, J. Atmos. Sci., 41, 1336-1355, 1984.

1 **Table 1.** Cloud optical thickness τ, effective radius r_e, and values of H_0 and S_0 for the eight

2 pixels highlighted in Fig. 1 (sorted by H_0). For pixels 5, 6, 7, 8, Fig. 3a shows the spectral shape

3 of H_λ.

Pixel	τ	r_e (µm)	H_0 (%)	S_0 (%/100 nm)
6	10.3	27.5	28.92	2.36
1	13.0	30.1	21.17	1.56
3	21.2	30.0	13.04	1.08
2	18.1	30.6	9.92	1.63
5	12.2	27.5	4.95	0.48
7	8.0	27.8	−5.18	-0.78
4	11.8	28.2	−18.7	−1.54
8	7.7	24.2	−24.13	−2.46
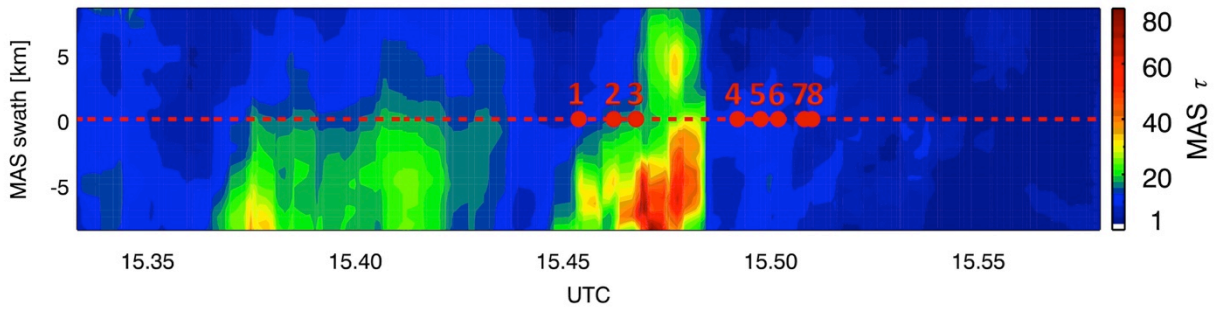
2 **Fig. 1.** Cloud optical thickness from MAS along an ER-2 leg from 17 July 2007 (length: 192 km,

3 swath: 17.5 km), re-gridded to a horizontal resolution of 500 m. The red dashed line indicates the

4 ER-2 flight track in the center of the MAS swath. Results of net horizontal photon transport for

5 the eight highlighted pixels are shown in Table 1 and Fig. 3a.
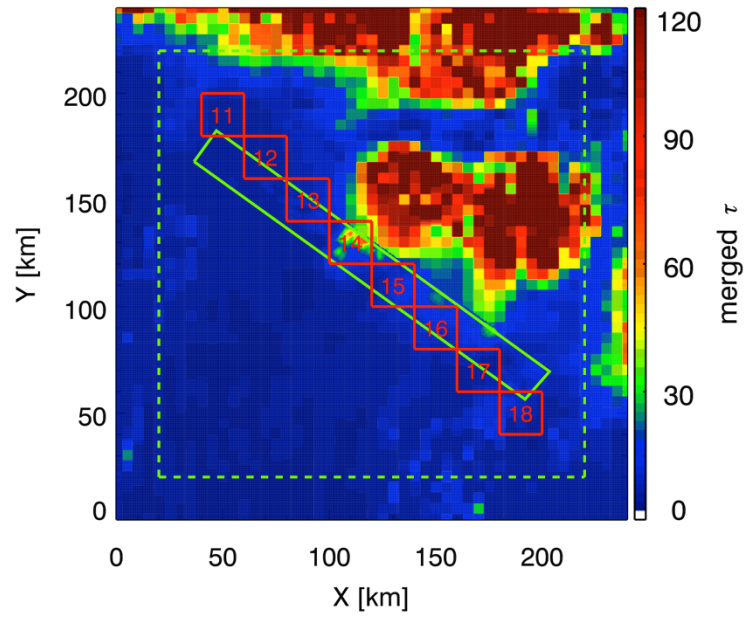
2 **Fig. 2.** Optical thickness of the large-scale cloud field. The green rectangle marks the embedded

3 MAS swath (Fig. 1); the red squares mark 20 km "super-pixels" within the scene. Radiative

4 transfer model output outside the dashed green square is discarded (see Section 7).
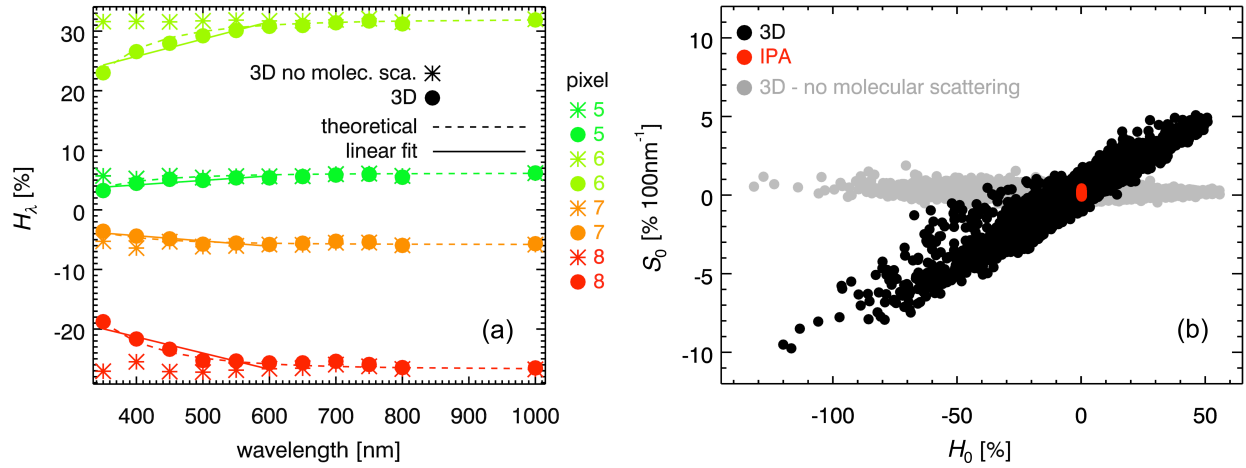
Fig. 3. (a) The H_λ spectra of pixels $\{5,6,7,8\}$ from Fig. 1 and Table 1 with ($\bullet$) and without ($\ast$) molecular scattering in the 3D calculations, as well as a fit based on Eq. (12) from Section 6 (dashed lines) and the simplified linear fit for obtaining S_0 (solid lines). (b) Spectral slope (S_0) vs. net horizontal photon transport (H_0) from (a) (both at 500 nm) for all the pixels from Fig. 1. Only 3D calculations with molecular scattering (black dots) show the systematic correlation between H_0 and S_0. Disabling molecular scattering (gray dots) incorrectly predicts a spectrally neutral (flat) H_λ ($S_0 \approx 0$ for all pixels). By definition, 1D calculations (IPA, red dots) do not reproduce net horizontal photon transport at all ($H_0 = 0$ for all pixels).
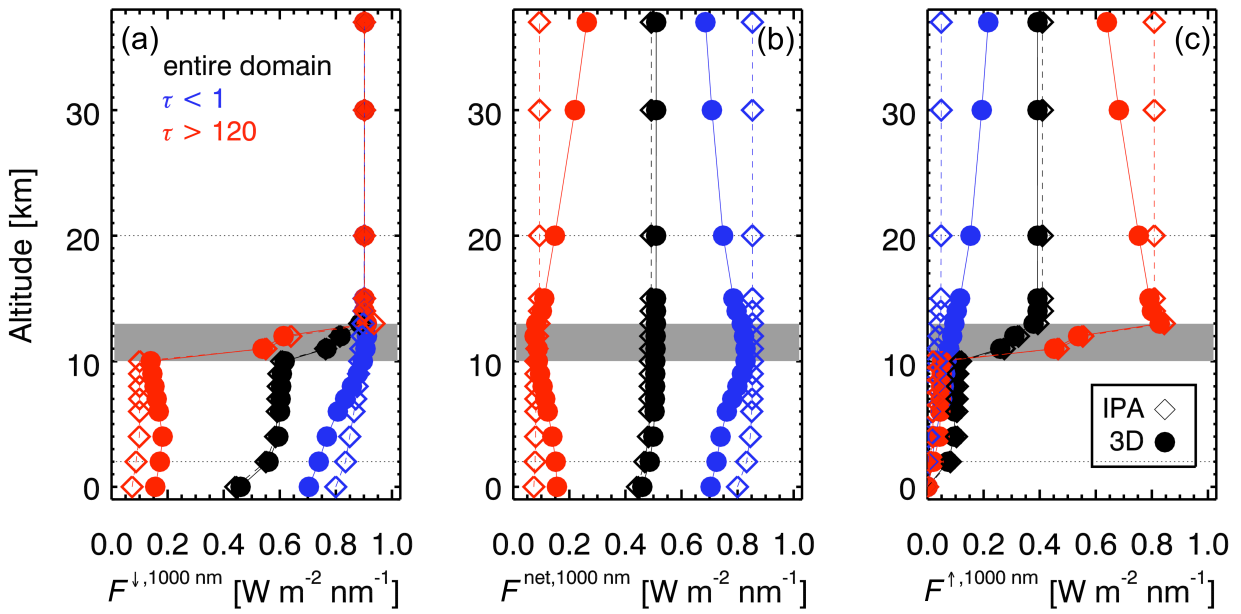
2 **Fig. 4.** Profiles of (a) downwelling, (b) net, and (c) upwelling irradiance at 1000 nm for the cloud

3 field from Fig. 1. The location of the cloud layer is marked in gray. Both IPA (dashed line,

4 hollow symbols) and 3D calculations (solid line, full symbols) are shown, averaged over the full

5 domain (black), over all columns with $\tau < 1$ (blue) and over columns with $\tau > 120$ (red).
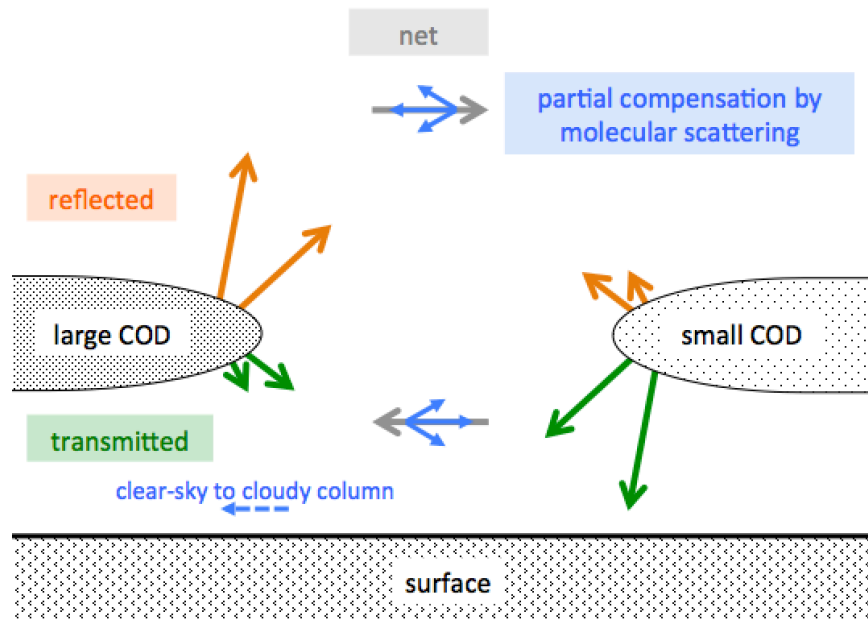
2 **Fig. 5.** Conceptual visualization of the mechanism of horizontal photon transport.
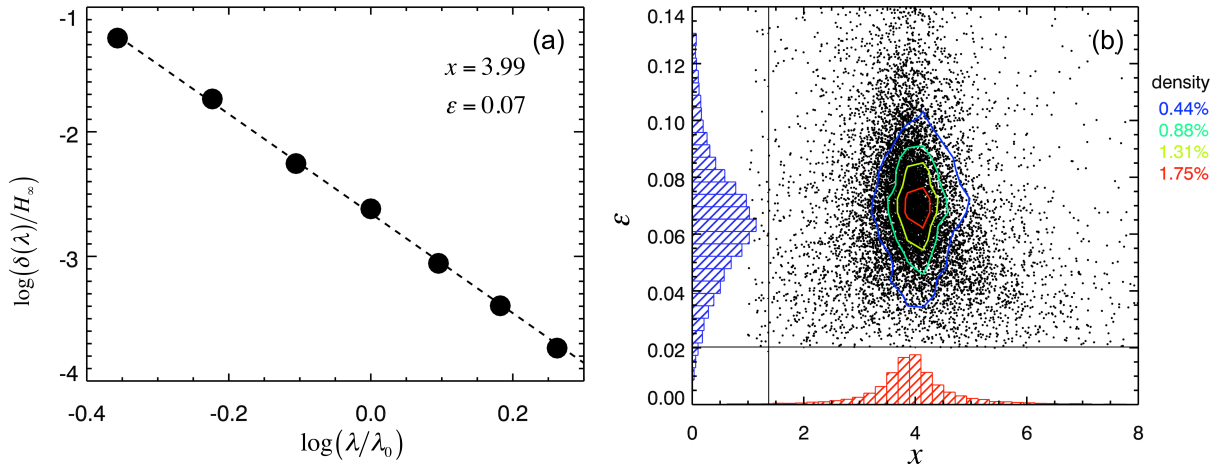
2 **Fig. 6.** (a) An example of the linear regression between $\log\dfrac{\delta(\lambda)}{H_\infty}$ versus $\log\dfrac{\lambda}{\lambda_0}$, from which the

3 values of x and ε can be derived. (b) The scatter plot of x versus ε for all pixels, joint PDFs $p(x,\varepsilon)$

4 (contours) as well as the marginal PDFs $p(x)$ and $p(\varepsilon)$ (histograms). The peak of $p(x,\varepsilon)$, and thus

5 the most likely $\{x,\varepsilon\}$ values for the cloud field is located at $\{3.85, 0.065\}$, and the domain-

6 averaged values are $\{3.91, 0.070\}$.
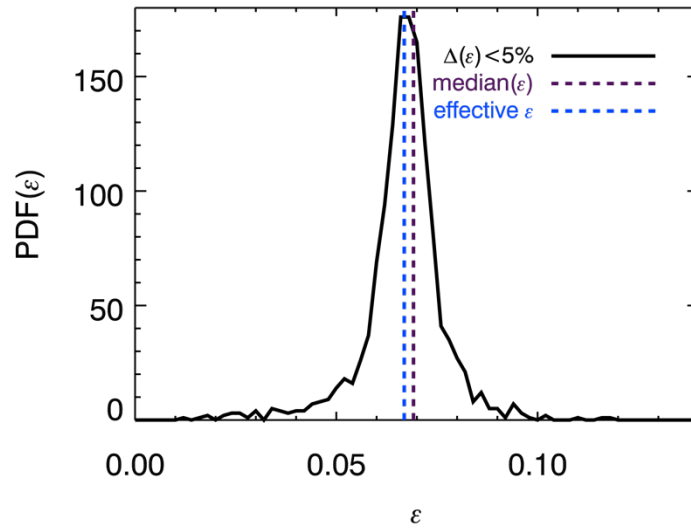
2 **Fig. 7.** PDF of ε for all pixels with $\Delta(\varepsilon) < 5\%$, median (purple dashed line), and domain-wide

3 *effective* ε derived from regression of S_0 vs. H_0 (blue dashed line).
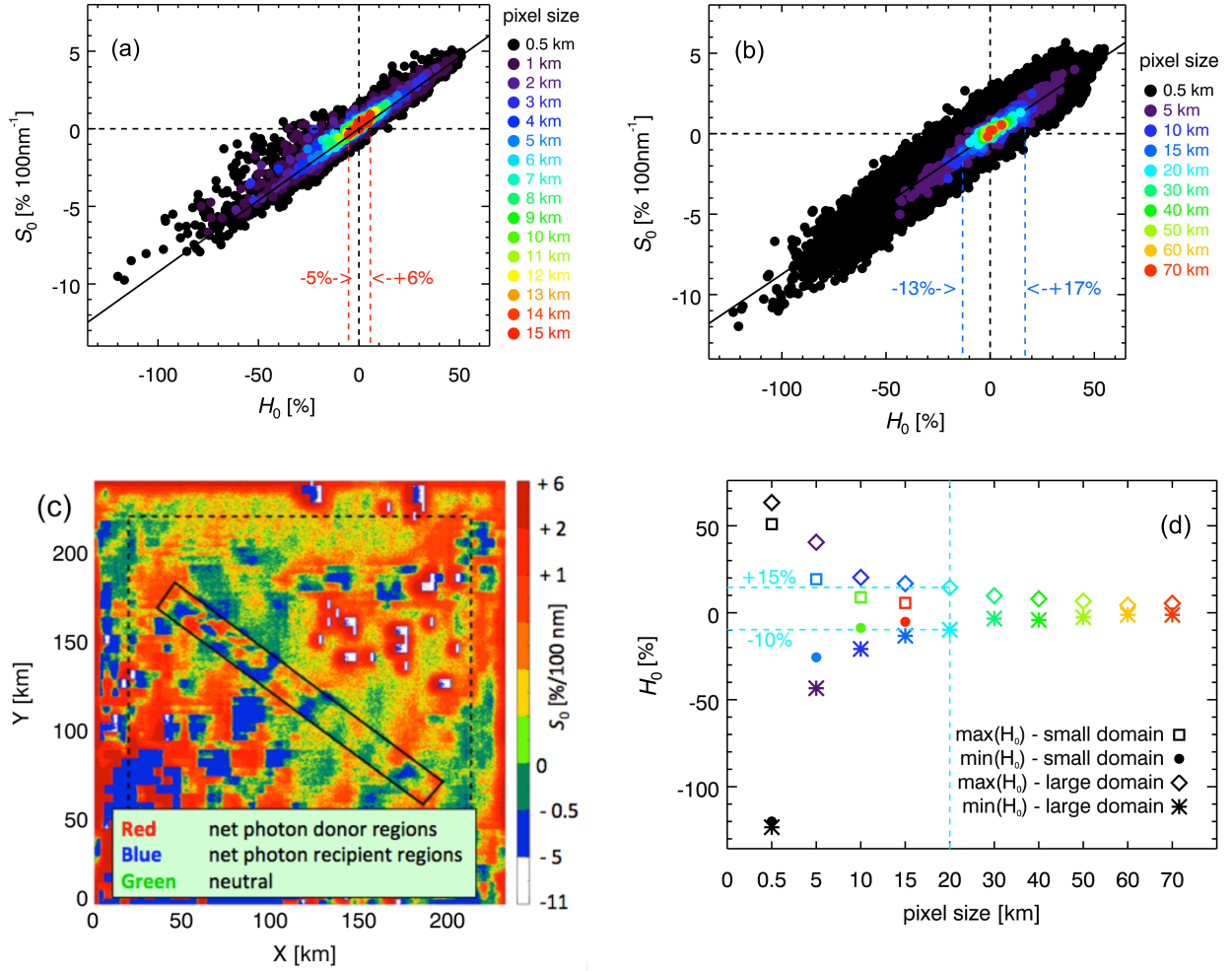
Fig. 8. Scatter plot of S_0 versus H_0 as obtained from linear regression of Eq. (12) for (a) the small domain from Fig. 1 and (b) the large-scale domain from Fig. 2, spatially aggregated to different scales, including the 20 km "super pixels" as highlighted in Fig. 2 (red squares). The dashed lines indicate the range for 15 km pixels. (c) Spatial distribution of S_0 from (b). Red (blue) indicates net photon "donor" ("recipient") pixels, and green "neutral zones" ($H_\lambda \approx S_0 \approx 0$). (d) Dependence of max(H) and min(H) on spatial aggregation scale (km). The color is the same as in (b).
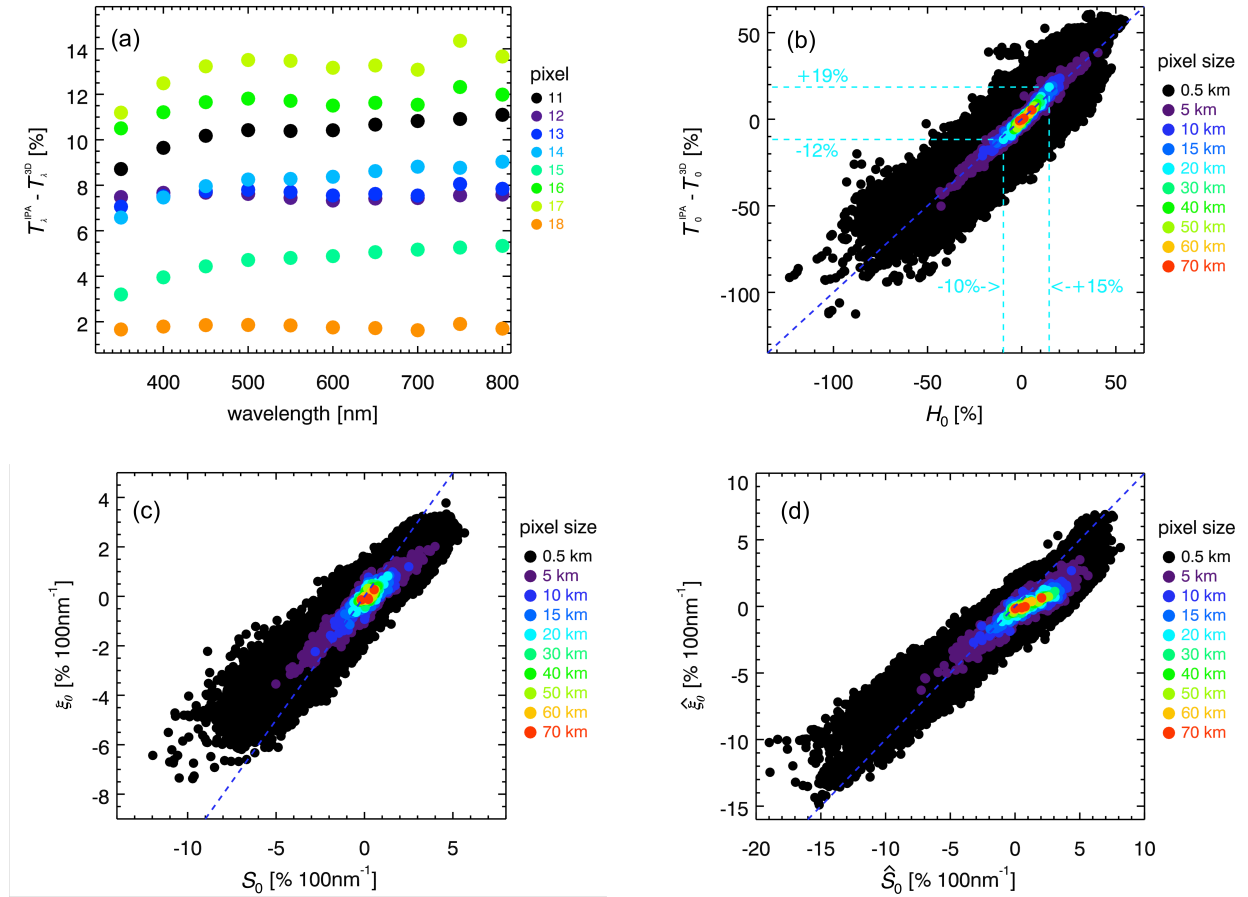
1   **Fig. 9.** (a) Transmittance biases (IPA-3D transmittance) for the eight super-pixels from Fig. 2. (b)

2   Correlation between net horizontal photon transport from Fig. 8b and transmittance bias for

3   multiple spatial aggregation scales. The dashed lines indicate the range of variability for 20 km

4   super-pixel size. (c) Correlation of the *slopes* of the quantities from (b). (d) Same as (c), but for a

5   bracket from the surface to cloud top, rather than the cloud layer only.
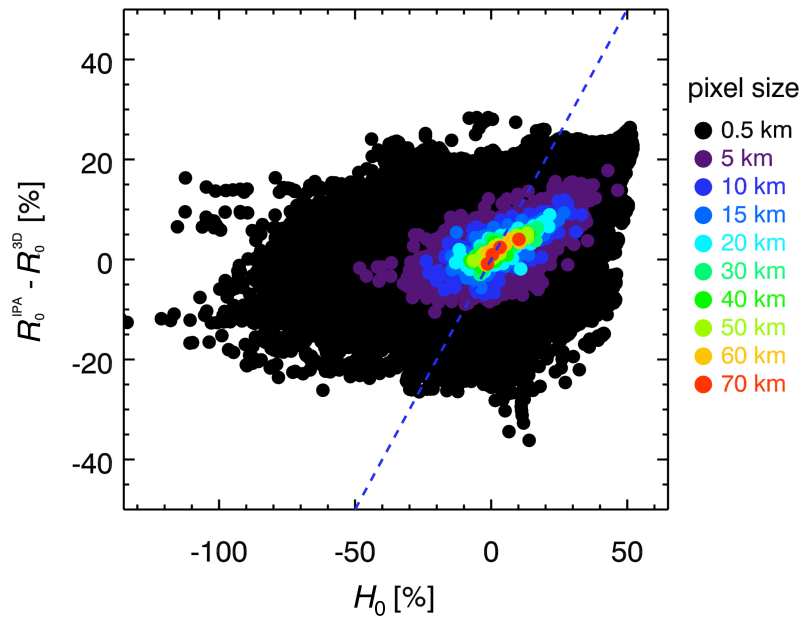
2 **Fig. 10.** H_0 is only weakly correlated with reflectance biases ΔR_0 (IPA-3D reflectance) at scales

3 below 15 km, which means that, statistically, biases introduced by horizontal photon transport

4 propagate primarily into transmittance, not albedo. This changes for larger scales.